



# A multi-method study of femtosecond laser modification and ablation of amorphous hydrogenated carbon coatings

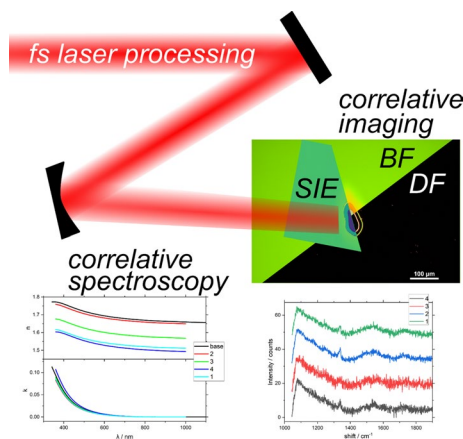
Kenta Hirahara<sup>1</sup> · Jörn Bonse<sup>2</sup> · Jörg Krüger<sup>2</sup> · Matthias Weise<sup>2</sup> · Elena Ermilova<sup>2</sup> · Robert Schusterbauer<sup>2,3</sup> · Andreas-Neil Unterreiner<sup>1</sup> · Andreas Hertwig<sup>2</sup>

Received: 27 June 2024 / Accepted: 7 October 2024  
© The Author(s) 2024

## Abstract

We present a study on femtosecond laser treatment of amorphous hydrogen-containing carbon coatings (a-C:H). The coatings were deposited on silicon wafers by a plasma-assisted chemical vapour deposition (PA-CVD), resulting in two different types of material with distinct properties (referred to as “absorbing” and “semi-transparent” coatings in the following). The samples were laser-treated with single fs-laser pulses (800 nm center wavelength, 35 fs pulse duration) in the ablative regime. Through a multi-method approach using topometry, Raman spectroscopy, and spectroscopic imaging ellipsometry, we can identify zones and thresholds of different fluence dependent effects and have access to the local dielectric function. The two coating materials react significantly different upon laser treatment. We determined the (non-ablative) modification threshold fluence for the absorbing coating as  $3.6 \times 10^{-2} \text{ Jcm}^{-2}$  and its ablation threshold as  $0.22 \text{ Jcm}^{-2}$ . The semi-transparent coating does not show such a low-fluence modification but exhibits a characteristic interference-based intra-film ablation mechanism with two distinguishable ablation thresholds at  $0.25$  and  $0.28 \text{ Jcm}^{-2}$ , respectively. The combination of tailored layer materials and correlative imaging spectroscopic methods delivers new insights into the behaviour of materials when treated with ultrashort-pulse laser radiation.

## Graphical abstract



**Keywords** Amorphous Hydrogenated Carbon Coatings · Correlative Imaging Measurement Techniques · Hybrid Metrology · Imaging Spectroscopy · Spectroscopic Ellipsometry · Ultra-short Pulse Laser Materials Processing

Extended author information available on the last page of the article

## 1 Introduction

Carbon is the chemical element with the largest variety of compounds possible because of its ability to bond covalently to itself and many other elements. This is not only true for molecular organic compounds, but also for carbon-based bulk and thin layer solids. The possibility of forming single and double bonds in different configurations, depending on  $sp^2$  vs  $sp^3$  orbital hybridisation and the presence of chemical aromaticity, produces a wide range of different properties. Often, carbon coatings are classified into the diamond-like, graphite-like, polymer-like, or rubber-like regime [1] [2]. While thin coatings of amorphous carbon materials were originally studied mainly for their mechanical properties with the aim of tailoring wear-protection coatings, interesting optical properties were found as well [3].

Plasma-assisted chemical vapour deposition (PA-CVD) from organic precursors is a very versatile tool to create carbon thin film coatings on a variety of substrates. The flexibility in the process parameters allows us to change the material properties in wide ranges easily and in an almost continuous manner. Consequently, all these coatings will contain hydrogen and, therefore, fall into the a-C:H category. One of their most interesting properties is that the  $sp^2/sp^3$  ratio and sometimes the hydrogen content can be varied, allowing to control some properties of the a-C:H material.

Because of the high hardness and brittleness it is often difficult to post-process and shape such coatings after their deposition to a carrier material (substrate). Here, contact-less laser irradiation provides unique advantages for processing coatings of varying thickness, particularly when ultrashort pulsed lasers are used. Because of high peak intensities and the pulse duration being shorter than typical electron-phonon relaxation times, ultrashort laser pulses enable a very precise structuring of almost any material, including hard carbon [4] [5]. Usually, they leave behind a minimum so-called heat-affected zone (HAZ) in the irradiated material, as compared to the often unwanted morphology when using longer-pulse lasers [6] [7] [8] [9] [10].

The residual modified material near the surface (in the HAZ) may have been affected by the strong electronic excitation of the a-C:H films. This eventually leads to the formation of a near surface ablation plasma: the early transient localised laser-excited electron plasma formed at the surface or within the films will certainly depend on the hydrogen and the optical properties content of the pristine film materials and can drive structural material modifications ( $sp^3$  to  $sp^2$  hybridised carbon bonds). On the other hand, the later ablation plasma contains neutral

or charged species (free electrons, atoms, ions, etc.) that may interact with the sample surface and can additionally change its properties (e.g. wetting, hardness, etc.). Thus, a detailed optical, structural, and topographic investigation of the laser-irradiated sample surfaces is desired [11] [12] [13] [14] [15, 16] [17].

In this work, we apply a multi-method characterisation of single-fs-pulse irradiation of two types of hydrogenated amorphous carbon films featuring sub-micrometre thicknesses and a significantly different  $sp^2/sp^3$  content ratio. Both types of layers are prepared in the same coating device using plasma-assisted chemical vapour deposition (PA-CVD) and characterised with ellipsometry. Optical microscopy (OM) in brightfield and darkfield imaging mode is combined with white light interference microscopy (WLIM), and micro-Raman spectroscopy ( $\mu$ -RS) which is a proven method to determine the molecular structure of carbon materials giving access to the  $sp^2/sp^3$  ratio [18] [19] [20] [21].

We used spectroscopic ellipsometry (SE) and spectroscopic imaging ellipsometry (SIE) to determine the dielectric function and layer thickness of the a-C:H material before and after laser treatment. This combination of different imaging and spectroscopic methods with morphological and topographic information enables us to identify laser-induced topographic, structural, and optical material modifications and allows to distinguish film- and ultrashort-pulse-specific ablation scenarios.

## 2 Experimental

### 2.1 Sample preparation by PA-CVD coating

The general strategy of this work is to fabricate two coatings with different optical properties but approximately the same thickness. Figure 1 shows the workflow we used together with photographs of the finished samples showing the differences in the optical properties seen with the bare eye. The green colour of the semi-transparent MW film is an interference colour. This effect is not present in the RF sample which is mostly opaque in the visible spectral range.

We deposited the different types of a-C:H coatings on 5 cm diameter, 0.5 mm thick Si wafers (<111> orientation, single side polished, n-B doping, delivered from Si-Mat-Silicon Materials e.K., Germany) The wafers were coated in as-delivered condition. After a short soft-etching step with RF Argon plasma for 30 seconds, a nominal targeted thickness of 500 nm a-C:H was deposited on each wafer. We used a CS730ECS cluster coating system from von ARDENNE Anlagentechnik GmbH (Germany) with a PA-CVD module from Roth & Rau AG (Germany). The system which was already used in our previous works on a-C:H coatings [3, 17, 22] is sketched in Fig. 2. The vacuum chamber contained

**Fig. 1.** Coating process used for preparing the samples in this study. The photographs show examples of the samples from the two different coating processes highlighting the transparent vs. absorbing properties

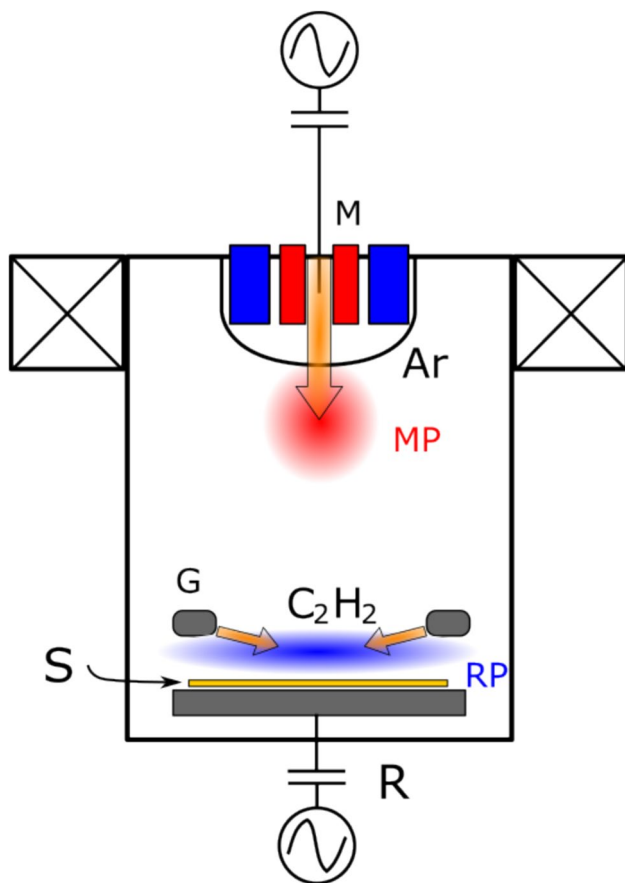
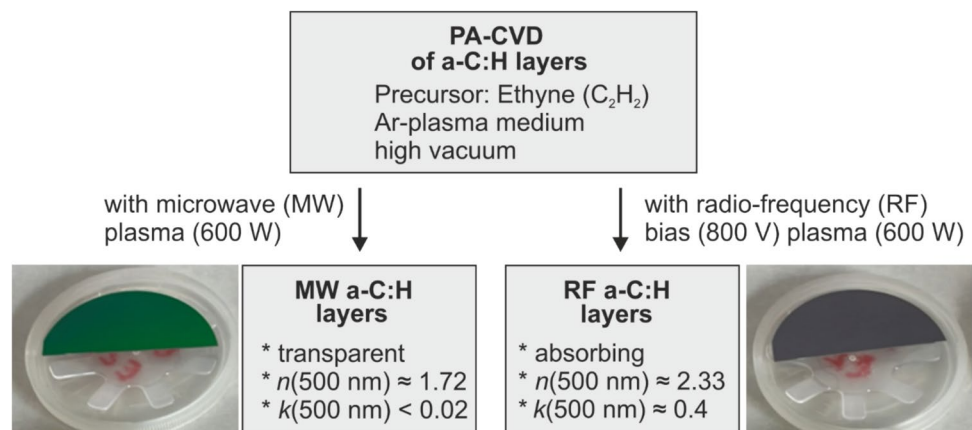


**Fig. 2.** Schematic of the PA-CVD reactor with the two independent plasma sources. The two process gases Ar and  $C_2H_2$  are injected into the vacuum chamber at different points. *S* sample, *M* MW emitter behind quartz cup, *G* ring-shaped gas inlet and electrode, *MP* microwave plasma, *RP* RF plasma, *R* RF power source. Orange arrows: gas flow of Ar and  $C_2H_2$

a sample holder and a ring-shaped gas inlet. We used the RF bias plasma source to coat pure RF-type coatings. This source was driven by a 13.56 MHz radio frequency (RF) generator with an automatic matching box unit. The vacuum

chamber was further equipped with a microwave (MW) plasma source, consisting of a 2.45 GHz microwave generator and an electromagnet control unit. We used this feature of the device for pure MW-type coatings. We denote the two different coating types resulting in these processes as “RF” and “MW” type layer throughout this text. Argon with 6.0 purity was the plasma medium and ethyne ( $C_2H_2$ ) with 2.6 purity was the carbon precursor gas for all coating processes.

The specific deposition conditions for the two different samples were as follows:

- RF:  $p = 4.5 \times 10^{-3}$  mbar, gas flow Ar: 20 sccm,  $\dot{V}(C_2H_2) = 40$  sccm.  $P = 600$  W,  $U = 800$  V.
- MW:  $p = 2.3 \times 10^{-3}$  mbar, gas flow Ar: 20 sccm,  $\dot{V}(C_2H_2) = 40$  sccm.  $P = 600$  W.

Here,  $p$  is the system pressure,  $P$  is the electrical power of the process,  $\dot{V}$  the gas flow rate, and  $U$  is the substrate bias voltage. After removing the samples from the vacuum chamber, we stored them under atmospheric conditions for several days before starting with the first characterisation experiments (mapping ellipsometry). This allows the layer material to stabilise as plasma-deposited carbon materials are still unstable and will react within the layer as well as with the atmosphere over several days.

## 2.2 Femtosecond laser processing of a-C:H coatings

Short pulses of 35 fs duration were provided by an Astrella laser system (Coherent, Germany) with a repetition rate of 1 kHz, emitting pulses at a central wavelength of 800 nm. The laser beam quality factor is specified by the manufacturer as  $M^2 \leq 1.2$ . Pulse on demand operation was successfully achieved using the single-shot mode of the laser system. For pulse energy control we used a Glan-Taylor polariser (Thorlabs, Germany) with an extinction ratio of  $10^5:1$ . Using this setup the polarisation state of the laser beam slightly changed in the lower pulse energy range. Therefore, we

generally don't correlate any effects with the laser polarisation state in this work.

To ensure identical conditions for each individual shot on different sample positions, we configured an optical system for calibration and experimentation, see Fig. 3. During calibration mode, the sample was substituted by a power meter to assess the average laser power, yielding a calibration curve by operating a linear polariser functioning as an attenuator. Simultaneously, we recorded the residual transmission through the focussing mirror in front of the sample with a photodiode and calibrated it to the results of the power meter at various pulse energies. This procedure ensured controlled energy conditions after replacing the power meter by the sample placed on a three-axis translation stage. Using the predetermined output of the photodiode (PDA100A2, Thorlabs, Germany) from the calibration, we recorded spatial coordinates, polariser angle, and photodiode peak voltage for each shot.

It is generally difficult to determine the beam geometry of focussed beams at the site of a laser processing experiment. For this reason, and because the beam shape is irregular in our case, we rely on determining the beam waist diameters from the damage threshold analysis by means of the  $D^2$ -method as described below.

### 2.3 Spectroscopic and imaging ellipsometry

A central aspect in understanding the laser-induced modification and ablation mechanisms here relies on the knowledge of the optical constants of the coating material before and – if possible – after laser irradiation together with the layer thickness. The most elegant method to determine these data is spectroscopic ellipsometry in single-point and

imaging form [23] [24] [25] [26] [27]. For thin films it is in many ranges of thickness and properties the only way to determine thickness and dielectric function at the same time. From the ellipsometric transfer data  $\Psi$  and  $\Delta$  depending on the wavelength  $\lambda$ , sample information like layer thickness  $d$  and the optical constants, i.e. the real ( $n$ ) and imaginary ( $k$ ) part of the refractive index can be determined by fitting a sample model to the measured data. From  $k$ , the absorption coefficient  $\alpha$  can be determined with this equation:

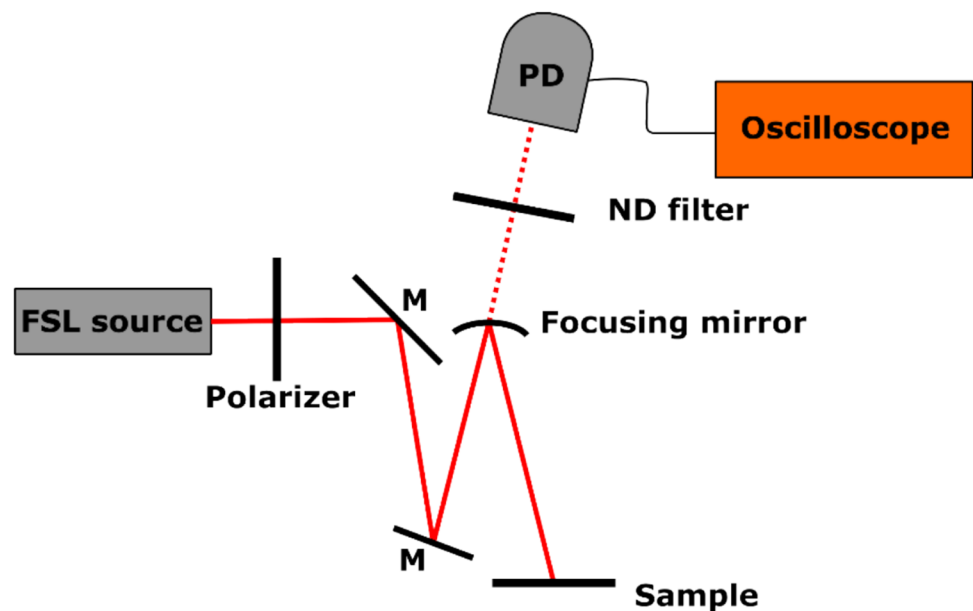
$$\alpha = \frac{4\pi k}{\lambda}, \quad (1)$$

together with the light penetration depth ( $\alpha^{-1}$ ).

We characterised both sample types (MW and RF) before the laser experiments by means of variable angle spectroscopic ellipsometry (SE) with a M2000DI instrument (J.A. Woollam, co. inc., USA) operating in a spectral range of 192 nm – 1697 nm and equipped with a mapping option. In all cases, three angles of incidence (AOI) of 65°, 70°, and 75° were used, respectively. This measurement recipe was applied to a rectangular scan pattern of 29 measurement spots evenly distributed over a circular wafer with 5 cm diameter. No beam focussing or shaping was applied. We recorded the ellipsometric transfer data  $\Psi$  and  $\Delta$  and did not assume special measurement parameters e.g., for the anisotropic case.

We performed spectroscopic imaging ellipsometry (SIE) measurements with an EP4 imaging ellipsometer from Park Systems (Germany) in a wavelength range between 360 nm and 1000 nm. We selected 40 evenly distributed wavelength values across this range and an AOI of 65°. The camera of the system delivered an image size of one megapixel and perspective corrected maps of  $\Psi$  and  $\Delta$  at each wavelength

**Fig. 3.** Schematic representation of the optical set-up for single shots on the samples. *FSL* Femtosecond Laser, *M* mirror, *ND* neutral density filter, *PD* photodiode



were produced by data analysis. This procedure resulted in 80 images for every measurement. All images presented in this work are focussed throughout and geometrically corrected to represent the true projected area of the camera sensor onto the sample surface, removing all defocussing and distortion introduced by the oblique angle of incidence.

For analysis, we defined regions of interest (ROIs) and calculated integrated extracts of each ROI for further analysis. This data extraction and image handling was done in the EP4 data studio software provided by the instrument manufacturer. Data analysis by fitting on all data (SE and SIE) was done in the EP4 modelling module as well as in the CompleteEASE software (J.A. Woollam) after converting the SIE extracted spectra to the required format. The correctness and consistency of SE and SIE was confirmed by calibration measurements.

#### 2.4 Characterisation of laser spots by optical microscopy, WLIM topometry, and mechanical stylus profilometry

The irradiated regions were inspected by an optical microscope (Nikon Eclipse L200, Japan) in brightfield and dark-field imaging modes using a white light halogen lamp for illumination along with a long working distance 10× or 20× microscope objective. For image acquisition and analysis, the Nikon software NIS elements (v. 5.42) was used.

To determine the topographic change after laser irradiation we measured surface topographies on the RF samples by means of white light interference microscopy (WLIM) with a Zygo NexView instrument (Zygo Corp., USA). The 2D data processing was done with the Zygo Mx software (v. 9). Our thin MW coated samples are too transparent for WLIM, so on these samples, tactile topometry was only possible with mechanical methods. For this, we used a Dektak XT profilometer (Bruker, USA) with a stylus radius of 2 μm and an opening angle of 60°.

#### 2.5 Characterisation of laser spots by μ-RS

Micro-spot Raman spectroscopy of the irradiated films was performed with an XploRA™ PLUS (HORIBA Europe GmbH, Germany) equipped with a 532 nm Nd:YAG-laser and a *x/y* piezo stage in backscattering geometry. The Raman spectra were taken by focussing the laser beam with a 100× (NA = 0.90) objective lens from Nikon. The theoretical laser

spot diameter of this configuration is 720 nm. The spectral resolution of the Raman spectrometer accounted to 0.98 cm<sup>-1</sup> for the transparent MW and to 1.6 cm<sup>-1</sup> for the absorbing RF coating. The laser processed spots were probed with Raman laser powers of 1 and 10 mW. Map measurements of the MW and the RF samples were performed using the point-by-point method using a spot-to-spot distance of 20 μm in both directions, with 8 accumulations and an acquisition time of 1 s and 2 s, respectively. A polynomial baseline fit was done to the acquired data in LabSpec 6 (HORIBA).

### 3 Results and discussion

#### 3.1 Thickness and dielectric function determined by spectroscopic ellipsometry

Table 1 and Fig. 4 summarise the mapping SE measurements. Apart from the semi-transparent layer dielectric functions developed for this work, we only used dielectric functions for semiconductor materials and their oxides from [28, 29]. All models of the a-C:H dielectric function use a multi-peak oscillator model as provided by the CompleteEASE analysis software. The idea of this modelling is to use an asymmetric peak function of the Tauc-Lorentz type for the overall shape of the dielectric function curve [30]. These functions are intended to be applied to amorphous semiconductor materials and are not fully applicable without modification to the present materials. Therefore, we used a Tauc-Lorentz function modified by a Gaussian sideband in the UV for the MW coatings. This material reaches a point with no detectable extinction coefficient within our measurement window. The absorption band of the RF coatings extends beyond the infrared edge of our measurement. Therefore, we modeled this type of layer by means of three E<sub>g</sub>-coupled Cody-Lorentz functions [31]. Both functions (Tauc-Lorentz and Cody-Lorentz) are asymmetrically modified variations of the complex Kramers-Kronig consistent Lorentz oscillator functions with a defined bandgap energy. The Cody-Lorentz form contains inter-band absorption making it better suited for the RF type coatings. The two different layer types clearly show strong differences in their dielectric function (Fig. 4A).

RF coatings show a much higher absorption (higher value of the extinction coefficient *k*) and a higher refractive index *n*. Both species show a decrease in *k* when approaching

**Table 1** Properties of MW and RF generated a-C:H coatings determined by spectroscopic mapping ellipsometry

Sample	<i>d</i> / nm	<i>d</i> range / nm	<i>n</i> (500nm)	<i>k</i> (500 nm)	<i>n</i> (800 nm)	<i>k</i> (800 nm)	$\alpha^{-1}$ (800 nm) / nm
MW	476.0	468–478	1.72	0.02	1.67	1.9*10 <sup>-4</sup>	>300000
RF	435.3	420–437	2.33	0.42	2.40	0.21	311



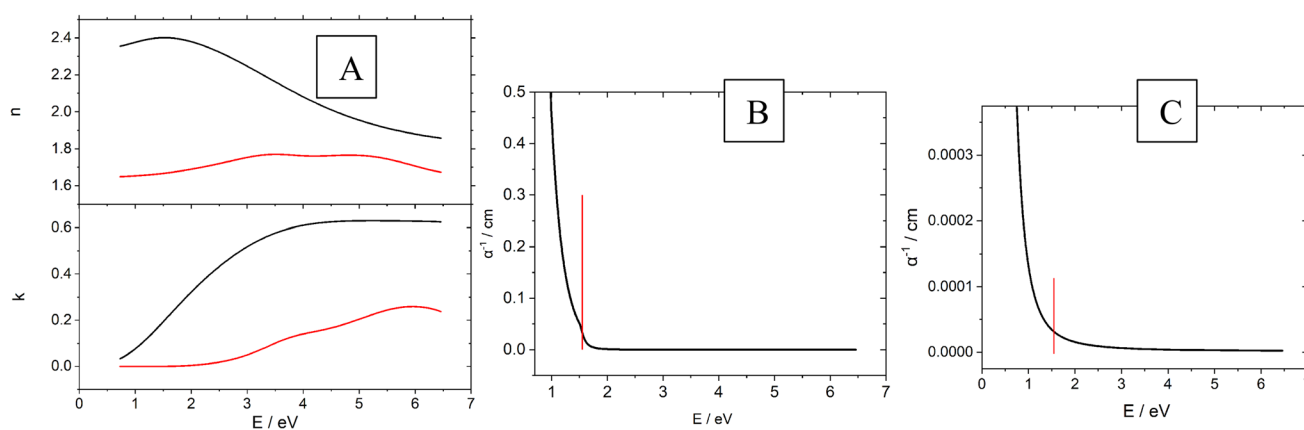


**Fig. 4.** SE analysis of a-C:H coatings A: optical constants of a-C:H coatings. Black: Real part ( $n$ ) and imaginary part ( $k$ ) of the refractive index of RF a-C:H. Red:  $n$  and  $k$  for MW a-C:H. B: Penetration depth

vs photon energy for MW a-C:H. C: Penetration depth vs. photon energy for RF a-C:H. In B and C the 800 nm wavelength is marked red

the near infrared. They essentially become transparent in the mid infrared making them interesting candidates for functional coatings in this wavelength region [3, 22]. The refractive index curves for the two materials show several interesting features. The absorption band of the RF material is unstructured, more intense and very broad, while MW a-C:H has two maxima at photon energies around 3.4 eV and 5.0 eV, respectively. Both materials reach the maximum of the absorption band within the observed spectral range and exhibit a decrease of  $n(E)$  towards higher photon energies (anomalous dispersion).

The layer thickness at the centre of the wafer substrate was determined to be 435.2 nm for RF, and 476.0 nm for MW, respectively. For the MW samples, we had to choose a slightly more complex model using an additional intermix layer of roughly 11 nm thickness between the a-C:H layer and the substrate. It is likely that such a layer also exists for the RF samples but is not detectable anymore because of the presence of the less transparent carbon layer. We performed mapping ellipsometry on both samples to determine the thickness homogeneity across the wafer. An inhomogeneous distribution of layer thicknesses and properties is common in some processes caused by an irregular shape of the plasma plume during the coating process. Table 1 lists the thickness ranges of the coatings for both cases. The overall thickness variation is in the range of 2% of the total thickness for RF a-C:H and 4% of MW a-C:H. While this cannot be regarded as a problematic inhomogeneity of a coating process for coatings of this thickness, it is important in the context of comparability when discussing the results of imaging ellipsometry below. The optical penetration depth ( $\alpha^{-1}$ ) at the laser wavelength is a relevant parameter which is determined using equation (1). As our fs laser source has a centre wavelength of 800 nm, we consider ( $\alpha^{-1}$ ) at this wavelength.

Figure 4 B and C show the  $\alpha^{-1}$  spectra of the two layer species, with the wavelength 800 nm marked. It is obvious, that the optical penetration depth differs between the two species with RF carbon showing a value for  $\alpha^{-1}$  of only 311 nm, while MW carbon has more than 0.3 mm, making the latter essentially transparent at 800 nm. The RF carbon, on the other hand, is highly absorbing (see  $\alpha^{-1}$  values in Table 1) with an optical penetration depth below the layer thickness. Therefore, these coatings are a showcase for back-reflection interference phenomena as predicted several times in the past for transparent coatings [6] [32, 33]. With the samples in this study, we should be able to detect this effect in the MW coatings, but not in the RF coatings. The difference in the optical properties of the formed coatings can be explained by the fact that the gas-phase reactions for the two plasma sources are fundamentally different [22]. In the case of the MW source, the distance between the plasma plume and the substrate is much larger than for the RF case. Therefore, the deposition mode for the MW coatings is also referred to as “collisional mode”, vs. the “non-collisional” mode in the case of the RF coatings. The additional space favours reactions of the products generated from the plasma-decomposition of the precursor giving rise to the formation of more stable molecules before the medium reaches the substrate. We assume this is the cause for the more polymer-like nature of the coatings generated by the MW plasma. These coatings are much softer and much more transparent than the RF-generated coatings. The latter coatings originate from a direct reaction of the atoms and molecules present in the plasma to form a more diamond-like structure. This is a good explanation for the different hydrogen contents,  $sp^2/sp^3$ -ratios, optical, and mechanical properties observed in the past.

### 3.2 Optical microscopy on laser treated spots

Optical micrographs of all spots were recorded both in brightfield and darkfield mode, with darkfield exposing the sharp rim of the ablated area for better distinction between ablated and non-ablated regions.

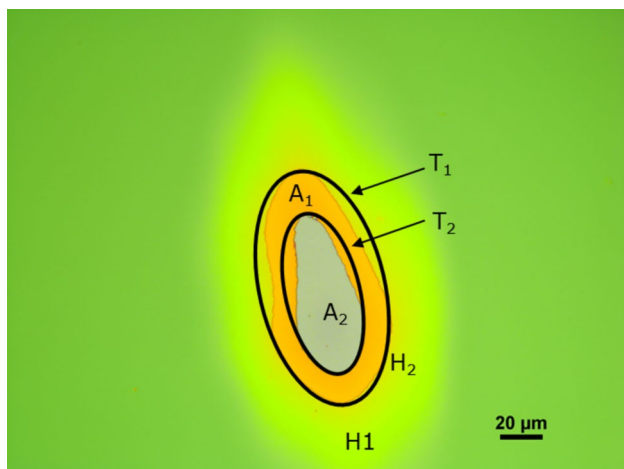


**Fig. 5.** Optical brightfield image of a laser spot showing all observed effects generated in this work - MW layer treated with a 90 μJ single fs laser pulse. H<sub>1</sub>: outer modified zone, H<sub>2</sub>: inner modified zone, A<sub>1</sub>: first ablation domain, A<sub>2</sub>: second ablation domain, T<sub>1</sub>: Elliptical fit to the threshold for A<sub>1</sub>, T<sub>2</sub>: Elliptical fit to the threshold for A<sub>2</sub>

Figure 5 shows an example of a spot exhibiting several different effects of ablation and modification. We identify different zones of modification and ablation. All ablation zones show a sharp rim, while the modification zone surrounding the ablation areas shows a smooth transition into the surroundings. Therefore, ablation and modification can be distinguished using darkfield microscopy, where ablation shows as a sharp bright line around the ablated zone. Note that the different colours in the ablation zones originate from thin film-interference effects of the residual a-C:H layer, depending on its local thickness, which indicates a step-like ablation profile. Figure 6 shows optical micrographs of selected laser treated spots. We show here collage images depicting the brightfield as well as darkfield images together. The brightfield images show the modified area without sharp geometric features while the darkfield shows the ablation rims very precisely. The different colours in the brightfield images of the MW spots show the two-step ablation occurring in this material which is not present in RF coatings. The modified area around the ablation crater can be detected for both materials with optical microscopy.

From the microscopic analysis, it can be deduced that the laser beam shows an irregular elliptical shape, making the damage threshold determination more difficult as in the case of perfectly circular or only slightly elliptical spots. The colours of the different ablation steps in the MW coatings are consistent across the series and the two zones can be found in every spot with sufficiently high pulse energy.

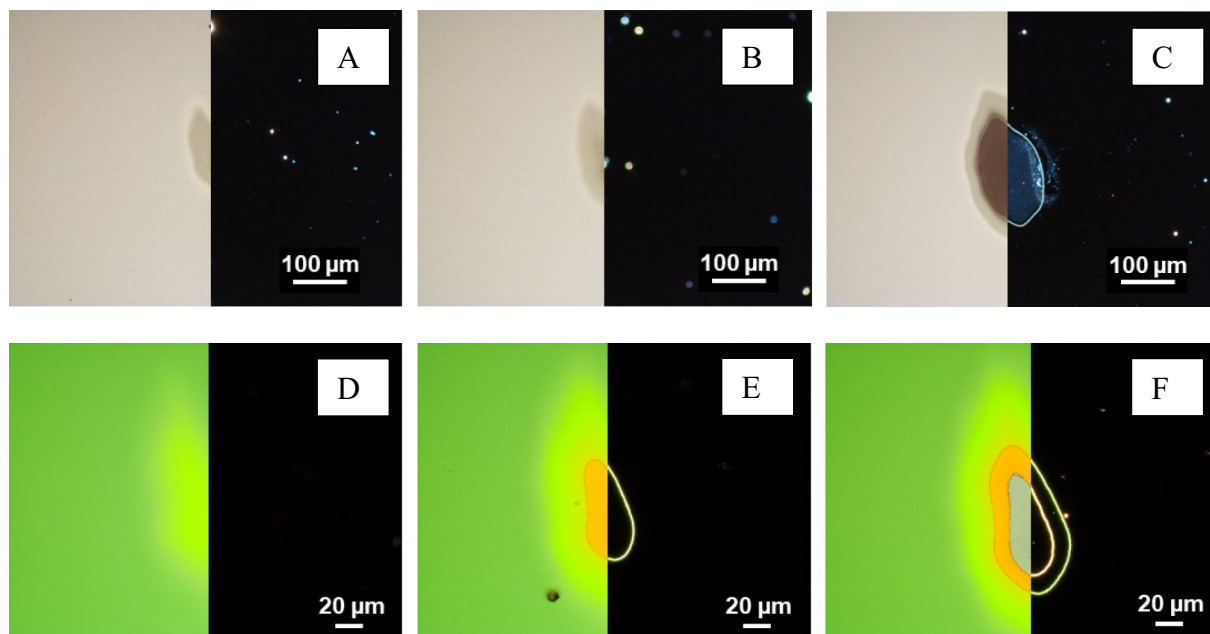


**Fig. 6.** Microscope image series of laser spots on RF (top row) and MW (bottom row) coatings at different pulse energies. The combination images (collages) show simultaneously both brightfield (left

side) and darkfield (right side) from the same location. The spot conditions are: **A:** RF, 80μJ; **B:** RF, 100 μJ; **C:** RF, 140μJ; **D:** MW, 80 μJ; **E:** MW, 90 μJ; **F:** MW, 100 μJ

### 3.3 Damage thresholds

We determined the damage thresholds by means of the well-established  $D^2$ -method by Liu [34]. Because of the irregular spot shape, we decided to fit an ellipse to each rim of the ablated zones. This method is demonstrated by the inserted ellipses in Fig. 5. This yields two values for the ablated diameter which then can be treated to calculate the threshold. In the case of the RF layer, there is only one ablation zone, while the MW coatings exhibit two different ablation thresholds. Table 2 shows a summary of the laser ablation thresholds and geometric features of this series of single-pulse irradiated spots.

The irregular beam shape generates two different sets of damage thresholds for the long and short axis because of the different slope in the  $D^2$ -analysis logarithmic fit. The values determined from the long and short axis can be seen as an upper and lower boundary for the true damage threshold for this reason. However, the beam diameters determined from this analysis are consistent. The threshold values of the RF material matches with what has already been found in [17]. Here, we observe an interesting fact: There is not much difference between the ablation thresholds in the two materials despite the fundamentally different optical properties. This can be understood in the context of the interference mechanism discussed below. Normally, the values for MW materials would be expected higher because of their higher transmission of the laser radiation. However, secondary effects can reverse this effect.

The ablation thresholds determined here for the a-C:H coatings are about an order of magnitude smaller than that of diamond which is  $sp^3$  hybridised ( $\sim 3.0 \text{ J/cm}^2$ , [35] [36]) for sub-50 fs Ti:sapphire laser pulses (800 nm) and even slightly smaller than that of graphite ( $\sim 0.3 \text{ J/cm}^2$ , [37]). The large difference to the ablation threshold of diamond arises from its large electronic band gap energy ( $\sim 5.5 \text{ eV}$ ) along with its high purity. Our a-C:H films, however, contain apart from  $sp^2$  and  $sp^3$  hybridised carbon also dangling bonds and hydrogen, which facilitate the electronic excitation by near-infrared fs-laser pulses and, thus, further lower the ablation threshold of our coatings.

**Table 2** Ablation thresholds  $F_{th}$  and  $\frac{1}{e^2}$ -widths  $w$  determined for MW and RF a-C:H. Indices 1 and 2 denote the first and second ablation

Layer type	$w_{1,long} / \mu\text{m}$	$F_{th,1,long} / \text{Jcm}^{-2}$	$w_{1,short} / \mu\text{m}$	$F_{th,1,short} / \text{Jcm}^{-2}$	$w_{2,long} / \mu\text{m}$	$F_{th,2,long} / \text{Jcm}^{-2}$	$w_{2,short} / \mu\text{m}$	$F_{th,2,short} / \text{Jcm}^{-2}$
RF	174	0.07	110	0.22	–	–	–	–
MW	156	0.10	103	0.25	150	0.13	104	0.28

### 3.4 Topography with WLIM and stylus profilometry

A full picture of the geometric changes of a laser treated surface requires topometric data. We use WLIM usually as the main method to determine topographic features of ablated structures, though we must use tactile profilometry for the MW samples. The reason for this is that the MW coatings are too transparent in the visible spectral range. The interferogram generated from a sample of a transparent material in the present thickness range contains double-interference patterns that cannot be converted into a useful topographic image by the standard method used in WLIM.

Figure 7A shows the results of the stylus profilometry of a 100  $\mu\text{J}$  single shot fs-laser treatment spot in MW a-C:H. This is the lowest pulse energy where the full ablation process with two distinct zones of different depth is observed in this material. Several features can be determined from this measurement. The modification zone outside of the ablation crater could already be observed in the microscope. The profilometry shows that in this zone the material is slightly expanded from the native state of the layer. This is usually explained by graphitisation causing a reduced density and therefore an increased volume of the material. While we have seen this effect already for RF-coatings [17], we observe it here for the first time in a hydrogen-rich hard polymer-like (MW) layer. The maximum height of this inflated zone is only a few nm. It can hardly be detected in the case of laser spots below the ablation threshold. The ablation can be divided into two zones with sharp edges to the unablated area and between each other. The outer zone appears orange in the brightfield optical microscope, while the inner zone shows a grey colour. When evaluating the depths of the two different zones, we obtain values in the range of 120 nm for the first (outer) ablation zone and 360 nm for the inner (second) ablation zone.

We define the thickness difference between the two ablated zones as the difference in height between the profile height of the first and second zone,  $h_{A1}$  and  $h_{A2}$ , respectively:

$$\Delta d = h_{A1} - h_{A2}. \tag{2}$$

The values of  $h_{A1}$  and  $h_{A2}$  are measured relative to the reference plane and after removing a linear baseline from the profile. Table 3 summarises the resulting values for all spots.

domain (only present in MW a-C:H). Indices short and long denote the respective value when the short or long axis of the ablated elliptical area is analysed



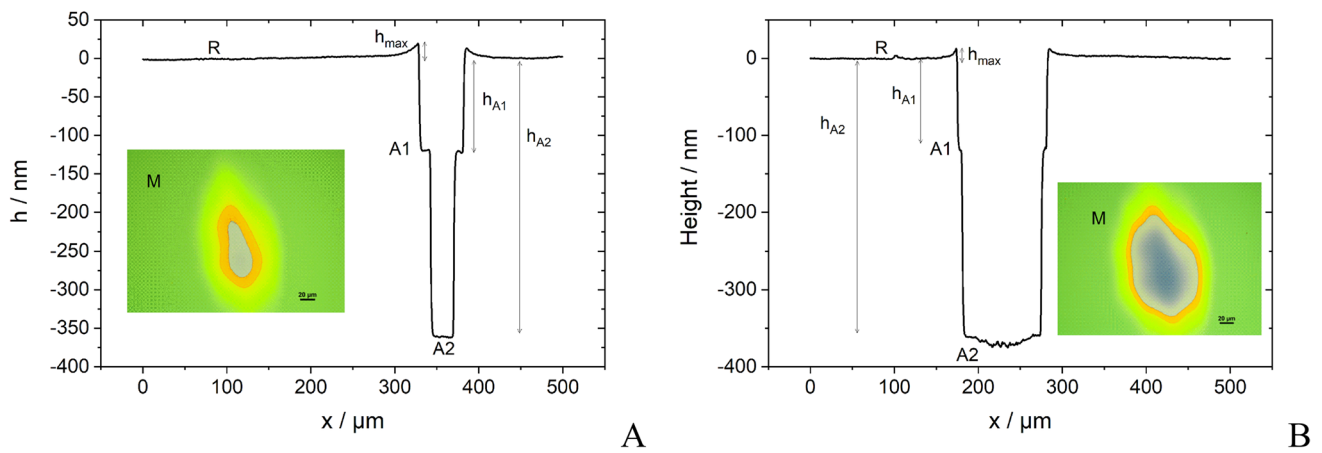


**Fig. 7.** Profilometric ablation depth determination of laser spots on MW coatings. **A:** spot treated with 100  $\mu\text{J}$ ; **B:** spot treated with 152  $\mu\text{J}$ . **M:** microscope image for comparison (scale bar is 20  $\mu\text{m}$  in

length), **R:** reference plane **x:** lateral position, **h:** height,  $h_{\text{max}}$ : maximum height, **A1:** first ablation area level with height  $h_{\text{A1}}$ , **A2:** second ablation area level with height  $h_{\text{A2}}$

**Table 3** Geometric features of laser ablated spots in a MW a-C:H layer, measured by mechanical stylus profilometry

$E / \mu\text{J}$	$h_{\text{max}} / \text{nm}$	$-h_{\text{A1}} / \text{nm}$	$-h_{\text{A2}} / \text{nm}$	$\Delta d / \text{nm}$
80	1.5	0	0	0
90	13.7	122	–	--
100	19.6	119	361	242
110	14.4	124	371	247
130	12.8	120	370	250
140	12.1	121	374	253
152	13.1	119	374	255

$E$  pulse energy;  $h_{\text{max}}$  maximum height of modified zone;  $h_{\text{A1}}$  height of first ablation zone;  $h_{\text{A2}}$  height of second ablation zone;  $\Delta d$  height difference between ablation zones

Interestingly, it is impossible to remove the a-C:H layer completely with the laser pulse energies available on our laser system. Such an effect was already observed for thin polymer films upon single fs-laser pulse irradiation [32]. The two laser-irradiated spots in Fig. 7, demonstrate this: The spot in Fig. 7A (100  $\mu\text{J}$ ) shows essentially the same depths (119 nm and 361 nm) as the one in Fig. 7B (116 nm and 370 nm) for the first and second ablation zone. At the same time, the sizes and areas of the ablation zones are consistent and allow for the  $D^2$ -analysis presented above.

Another interesting effect lies in the values of these ablation depths for different zones. In [6], intra-layer interference enhanced ablation is discussed which leads to certain preferred ablation depths in transparent coatings. In the case of our MW coatings, we expect this because the penetration depth at the laser wavelength is very high (i.e. the material is practically transparent), the interface to the substrate has a high refractive index contrast, causing a high reflectivity, and the thickness of the layer is in the right range (larger

than  $\lambda/2$ ). From the findings in [6], the difference between the two ablation levels is predicted as

$$\Delta d = \frac{\lambda}{2n}, \tag{3}$$

as the distance between two intensity maxima of the standing light wave caused by the counterpropagating incident fs-laser radiation and the wave reflected at the film/substrate interface should be half of the wavelength in the medium. With  $n = 1.67$  at  $\lambda = 800 \text{ nm}$  ( $E = 1.55 \text{ eV}$ ), as determined from the SE analysis, we expect  $\Delta d = 238 \text{ nm}$ . The value for  $\Delta d$  in all spots of this series is between 240 nm and 255 nm with the smaller values for irradiation with less energy. We consider this an excellent match and an impressive confirmation of this effect. The lower geometric minimum at higher pulse energy can be explained by secondary effects like evaporation of additional material. This fits the observation that the bottom of the ablation crater has higher roughness and a curved shape for higher energies, as can be seen in the right image in Fig. 7.

The situation is different for the absorbing RF coatings. Figure 8 shows the results of WLIM topography analysis on laser spots on this layer material. It is apparent that the effect of laser treatment of this material is much more dominated by material modification than ablation. Even far below the ablation threshold, the mass density decrease from the graphitisation process causes the formation of small bumps on the layer surface with a height of several 10 nm. Once the ablation threshold fluence has been reached, the top of these bumps is removed by ablation, and a crater is formed with a sharp rim as in the MW samples. Again, even the maximum possible pulse energy is not capable of removing the layer entirely and in the case of RF coatings, the ablation crater does not even reach the original height level of the layer

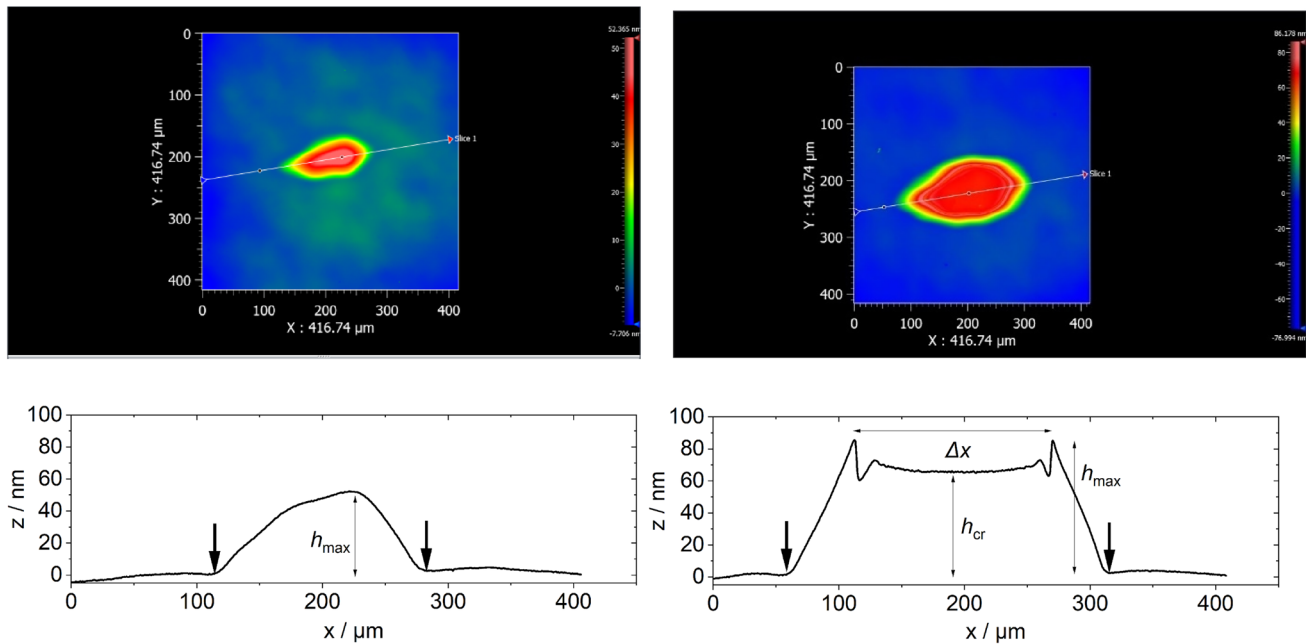


**Fig. 8.** WLIM images (top row) and the connected long elliptical axis profiles (bottom row) of RF spots. Left: 60  $\mu\text{J}$ , right: 100  $\mu\text{J}$ . Bold black arrows identify the bump onset used for determining the modification threshold

**Table 4** Geometric features of laser spots on RF (absorbing) coatings

$E / \mu\text{J}$	$h_{\text{max}} / \text{nm}$	$h_{\text{cr}} / \text{nm}$	$\Delta h_{\text{cr}} / \text{nm}$	$\Delta x / \mu\text{m}$
60	50	–	–	163
70	90	–	–	198
80	83.5	64.6	18.9	219
90	113	–	–	221
100	83	63	20	252
110	89	71	18	263
130	90	75	15	296
140	85	67	18	301
152	88	64	24	308

measured by WLIM:  $E$  pulse energy,  $h_{\text{max}}$  maximum height on the rim measured from reference;  $h_{\text{cr}}$  height in the centre of the crater, measured from reference;  $\Delta h_{\text{cr}}$  maximum depth of crater measured from rim height,  $\Delta x$  maximum length (large axis size) of the modified zone

surface. We have shown in the past how precise height and volume measurements of laser spots can be used to gain insight into the mechanism of ablation [17]. The curvature of the substrate-layer system due to intrinsic stress has to be taken into account for this analysis to be correct [38] [39].

The additional geometric features determined from WLIM are summarised in Table 4. We observe a steady increase in the bump height as well as the ablation depth with increasing pulse energy. The 2D WLIM profiles, allow us to determine the modification threshold by measuring the locations of the modification bump's onset i.e., the last point

in the cross-section line profile still at unmodified surface level. The points are indicated in Fig. 8 by bold black arrows. The distance of these two points on every profile curve gives the large axis diameter of the modified zone. This transition cannot be determined simply from microscope images as it is blurred in the image. It also cannot be measured by profilometry or AFM as the laser distances are too large for AFM and profilometry does not allow an accurate crosscut along a specific line.

The values can be used as basis for a  $D^2$ -analysis analogue to the ablation crater above. The result for the long-axis modification threshold is a threshold of  $F_{\text{th}} = 3.6 \times 10^{-2} \text{ Jcm}^{-2}$  at a long axis  $\frac{1}{e^2}$ -radius of the beam of  $w_0 = 195 \mu\text{m}$ . The value for  $w_0$  matches with the respective values for the long axis for the ablation craters of the shots on the absorbing RF coatings (see above).

### 3.5 Mapping micro-Raman spectroscopy

Figure 9 shows two examples of Raman spectra taken on transparent (MW) and absorbing (RF) material after laser treatment. To produce these spectra, we define a regular grid of measurement points on the area where the spots are located and measured at each point. The sum spectra depicted in the figure are then generated by averaging over a selected number of points. The curve graphs in the figure show the curves after simple automatic baseline-correction. The difference in intensity comes from this data

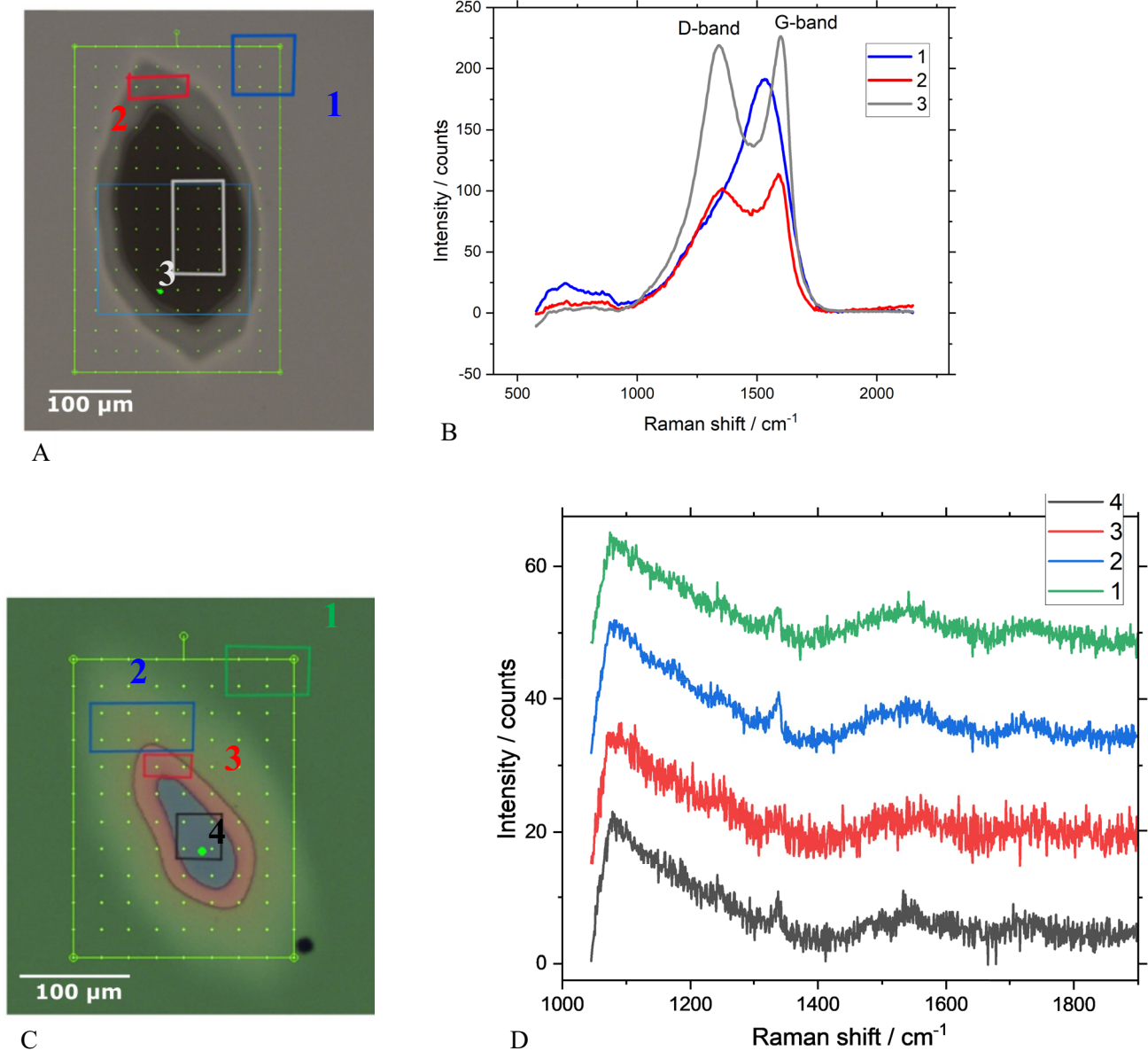


**Fig. 9.** Raman spectra and location of averaged regions for a laser spot on RF treated with 152  $\mu\text{J}$  (A, B) and a on the transparent MW coating treated with 100  $\mu\text{J}$  (C, D). The numbers and colours in the graphs (B, D) correspond to the numbers and colour frames in the

microscope images (A, C). The two distinct bands in graph B are labelled according to the D/G band nomenclature used in [22]. The curves in graph D are stacked in y direction by 15 units each relative to curve No. 4 to be distinguishable

processing step. The raw data after measurement show a much higher absolute intensity for the MW sample than for the RF sample.

The Raman measurements on the RF material (Fig. 9A) confirm the behaviour that has been found in the past [17] [22] [40] [41] [42]. The Raman spectra of carbon species are often discussed by identifying the D (“disorder”) and G (“graphite”) bands. Both bands are usually present in carbon coatings like the absorbing carbon material. The effect of

graphitisation on the material is prominently visible in the spectrum as both bands shift to higher frequencies, become narrower, and the intensity ratio  $I(G)/I(D)$  increases. We can reproduce all of these effects confirming that the previously developed microscopic models explaining the laser modification of a-C:H coatings on the basis of Raman spectra are applicable to this material [43] [44]. The most important changes this model proposes are a decrease in  $\text{sp}^3$ -carbon, an increase in  $\text{sp}^2$ -carbon, and the formation of a higher-ordered

phase within the layer. All of these effects can be determined readily by analysis of Raman spectra [45, 46].

The MW a-C:H layer material reveals a different behaviour in both states, treated and untreated than its RF counterpart, as can be seen in Fig. 9B. These coatings are much less accessible for Raman spectroscopy. While the overall scattering intensity is larger, the spectra are much more noisy and practically featureless in the amorphous carbon range. The reason for this is the high transmission for the excitation wavelength of the MW compared to the RF material. Basically, we record off-resonance Raman spectra for MW and resonant spectra for RF carbon. Despite this issue, there is information in the spectra and several assertions can be made about the MW material from the spectra. The scattering signal of MW a-C:H carbon is much more superimposed by fluorescence. The region between  $1400\text{ cm}^{-1}$  and  $1600\text{ cm}^{-1}$  shows a very broad peak similar to the double peak structure visible for RF carbon. The peak is much weaker which matches the assumption of a more polymer-like nature for this material. After baseline subtraction, it becomes apparent that this peak does not change at all after irradiation. The peak frequency, peak width, and shape, stay the same. The whole series of spectra recorded for this material are identical. The raw spectra (not shown here) scale only slightly with the smaller layer thickness in the ablated region. Therefore, we can determine no significant change in the spectra of MW a-C:H before and after laser treatment and between the two different ablation domains. This indicates that the processes observed for the RF material do not occur here. The laser modification of the MW a-C:H material does not change the chemistry or morphology of the

irradiated layer enough to cause an effect visible in Raman spectroscopy.

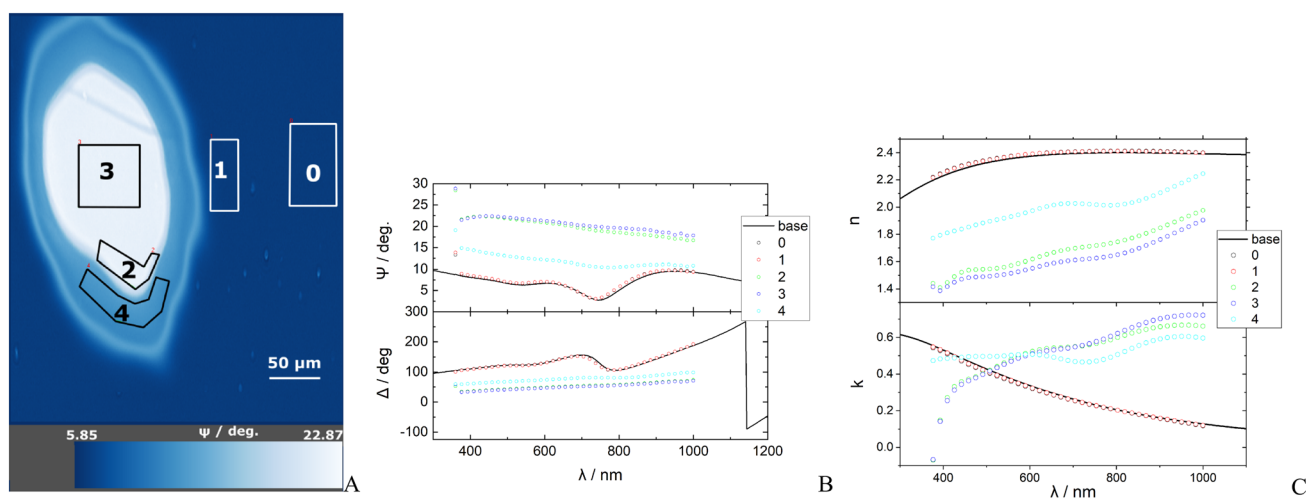
### 3.6 SIE of laser spots

As the SIE measurement yields full ellipsometric spectra for each pixel of the resulting images, it can be analysed after the measurement by defining arbitrary regions of interest (ROI). An averaged spectrum – “pixel shot” – over one or several ROIs can be calculated in this way. For easy re-use of models, we transferred these data to the software used for SE for further analysis. Special care must be taken when modelling because the SIE data is much less extensive than the SE data. We determined consistent models by merging the data from SE and SIE.

Figure 10 shows the result of such an analysis. Part A of the figure shows the location and shape of five different ROIs. The ROIs are on the untreated surface (ROI0), near the modified area (ROI1), in the outer part of the ablated area (ROI2), in the centre of the ablated area (ROI3), and in the modified, non-ablated zone (ROI4).

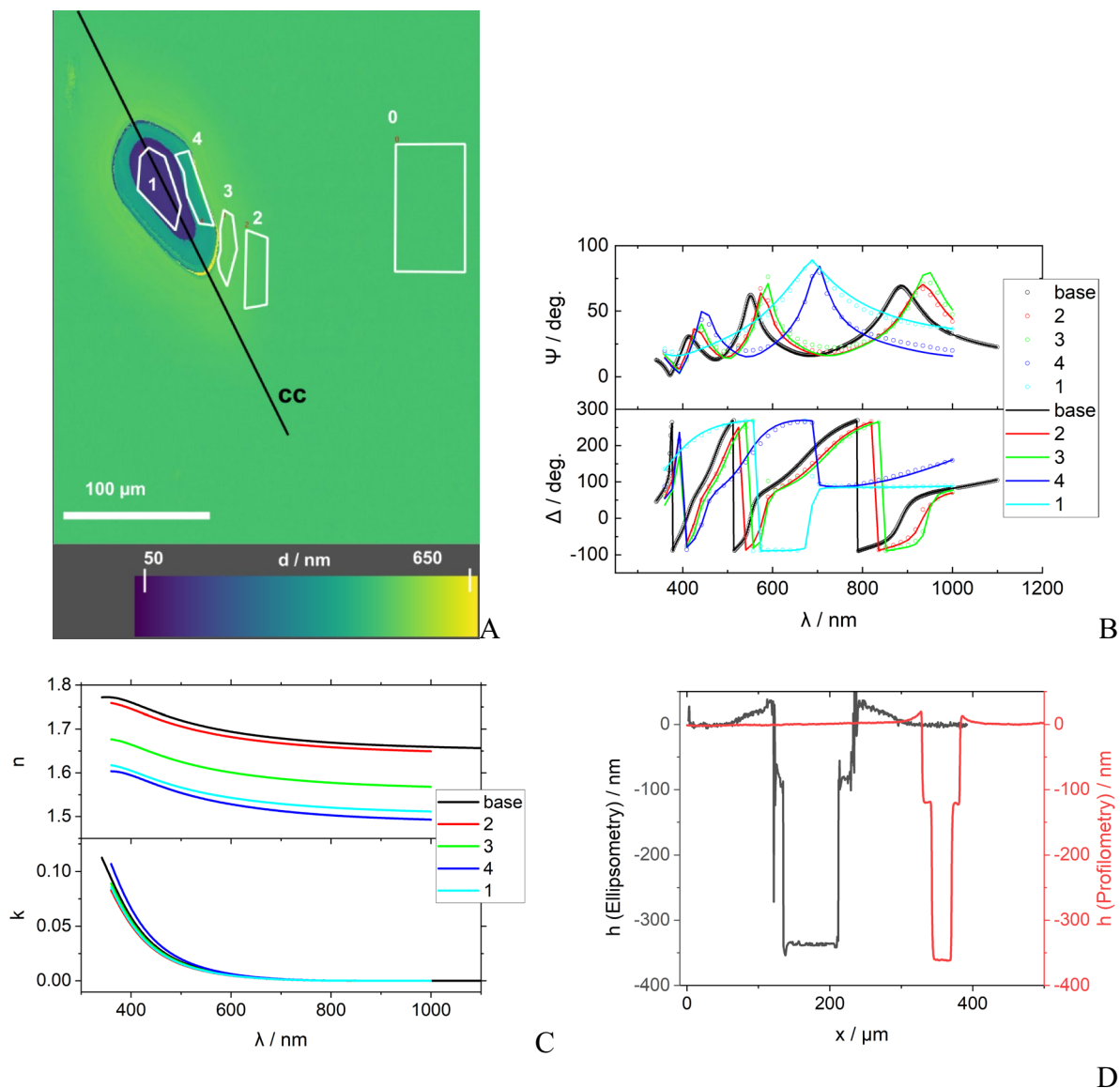
In Fig. 10 and in Fig. 11, we include data from the SE analysis using the M2000DI instrument, denoted as “base” curve in both cases. This data has a larger wavelength range than the SIE data. We compare all measured and modelled ellipsometric spectra with this result. It is expected that the data from the untreated region (ROI0 in all cases) will be very similar.

Figure 10B shows the ellipsometric spectra from the pixel-shot and the base measurement for comparison. The raw data correlation between SE and SIE is very good,



**Fig. 10.** Results of the SIE analysis of a high-energy laser spot (130  $\mu\text{J}$ ) on RF (absorbing) a-C:H and comparison with the results from SE on the untreated layer. **A** Colour code image of  $\Psi$  at 540 nm. The black / white lines indicate the different ROIs and the numbers denote the respective ROI number in the analysis. **B** Ellipsometric

data  $\Psi$  and  $\Delta$ . The curve denoted “base” is the SE data from the SE measurement for the untreated layer. The numbers denote the respective ROI number. The lines in the same colour depict the calculated data from the model **C** Modelled values of  $n$  and  $k$  for the base measurement and the different ROIs



**Fig. 11.** Analysis of SIE data for a mid-energy laser spot on MW a-C:H. The pulse energy was 100  $\mu\text{J}$ . **A** Imaging ellipsometry map, result of pixel-by-pixel fit (Thickness  $d$ ). The white shapes mark the different ROIs. The numbers denote the numbering of the ROIs which is also used in the curve graphs. The black line labelled cc marks the cut line for the profile plot **B** measured (dots) and modelled (lines) ellipsometric data  $\Psi$  and  $\Delta$ . The black curve and dots

are the base material data produced before laser treatment with the M2000DI ellipsometer. The data at ROI0 is identical to ROI2 and not shown here for clarity. **C** optical constants at the different ROIs from the model fit. **D** comparison of the profile from ellipsometry and the profilometer. The height from the ellipsometer is calculated by subtracting the total layer thickness from the local layer thickness from imaging ellipsometry

slight differences can be explained by the initial inhomogeneity of the layer. The layer thickness obtained for ROI0 is 431 nm compared to 438 nm for the untreated layer. As explained above, we usually analysed the untreated coatings with a multi-peak function. This is not possible for the laser-treated RF spots, as the dielectric function of the material in the spot is too far away from the unmodified state and the difference in transparency for the different material prevents the use of the same model. Additionally, the modified material is so highly absorbing over the whole observable

wavelength range that the ellipsometry measurement does not recognise this material as a layer but as a bulk material making it impossible to determine the layer thickness from ellipsometry.

We modelled the modified material using a spline model with enforced Kramers-Kronig consistency for the carbon layer dielectric function [47–49], allowing for an easier modelling. In Fig. 10C, the result for the different modified and/or ablated zones are depicted. Obviously, the value of  $k$  increases above 500 nm and decreases below this



wavelength. Simultaneously,  $n$  decreases over the whole spectrum. Because of graphitisation, the whole absorption band shifts towards the infrared and the trend of  $k$  with wavelength changes: for the modified material,  $k$  increases with increasing  $\lambda$ . We see this change as a typical effect for graphitised carbon coatings. It could be directly observed here for the first time on a microscopic length scale for single-pulse laser modified materials. Another important result can be obtained from the fitted data for ROI4. This location represents an outer region of the modified zone. The optical constants show an intermediate stage between unmodified and modified a-C:H material. The fit does not contain a good value of the layer thickness, so we cannot correlate the thickness determination from ellipsometry with the topometry measurement in the case of the laser-treated RF material.

We performed the same analysis for the spots on MW a-C:H coatings, as shown in Fig. 11. The conditions to obtain a full ellipsometric fit analysis are better in this case because of the higher transparency of the material. Therefore, we were able to fit the ellipsometric data at different ROIs with the same model that we used for the initial material without the necessity to change the model. This model also yields the local layer thickness as a fit parameter. The fit curves in Fig. 11B and C show pixel-shot curves from the different ROIs of the measurement together with the corresponding fit data. The respective ROIs are depicted in Fig. 11A over a map of the layer thickness  $d$  in nm, calculated pixel-wise from the same measurement.

Figure 11B shows the integrated ROI ellipsometric spectra as dots together with the respective fit curves as solid lines. The match between experiment and fit is good for all ROIs. The thickness of the layer in the untreated area (ROI0 and 2) is different from the base value because of the different location. Figure 11C depicts the optical constants for the different ROIs. The key values of the fit are summarised in Table 5. The results for the extinction coefficient  $k$  are unsystematic and the differences in this parameter between the different locations are very small. We therefore do not

consider these values to be relevant, their uncertainty is larger than the range of their values.

The refractive index  $n$  shows a shift from higher values for untreated or outer locations to lower values in the centre of the ablation crater where the second ablation region is located. The overall shape of the curves for  $n$  does not change between treated and untreated material. This is a clear indication that MW a-C:H coatings are not altered in the same way by laser irradiation as their RF counterparts. This change can be explained solely by a variation in density of the material.

The local a-C:H layer thickness is the most significant result of this analysis. For the MW sample, a pixel-by-pixel fit procedure was possible. Figure 11A shows the resulting map of the layer thickness together with the ROIs and a cross-section line. Using the thickness values along this line, we can compare the local layer thickness with the geometrical values from the profilometry measurement. In Fig. 11D, this comparison is shown, the height values are obtained by subtracting the total layer thickness from the SE analysis from the local thickness. The close agreement between the two methods is apparent. The ellipsometry measurement tends to produce higher thickness values than what is expected from profilometry and has a larger noise level because each single fit uses the spectrum from only one pixel. For the comparison in Table 5, we therefore use the values produced from the pixel shots as they average over more data and therefore have a lower uncertainty.

We see no indication for other effects than discussed so far. Spallation and blistering are often discussed when hard thin coatings are processed by lasers, but in this case, this would be clearly visible in the ellipsometric data. Therefore, we can be sure that we observe only material modification and ablation. The MW a-C:H layer material shows signs of changing its density without changing any of its structural features as can be concluded from the change in the refractive index. Raman spectra support this explanation as they do not show a significant change in the modified or ablated zones of MW coatings which is a different finding than for RF a-C:H showing the typical spectrum change for graphitised amorphous carbon. This finding is different from other laser treatment studies, e.g. the ones described in [50]. In the latter work, indication was found for spallation as well as blistering for coatings very similar to the MW a-C:H material investigated here but coated on a substantially different substrate – glass – and using a different laser – 532 nm, ns pulse duration instead of 800 nm, fs duration. Apart from the morphological differences, the microscope images in the older work hint at a darkening effect associated with graphitisation which we could not find in the present work.

This is a good example that the outcome of laser treatment may change drastically when the conditions are varied.

**Table 5** SIE fit results for the MW a-C:H laser spot at 100  $\mu\text{J}$  pulse energy

ROI No.	Thickness $d$ / nm	Thickness from profilometry $d_{\text{pr}}$ / nm	$n$ @ 400 nm	$n$ @ 800 nm
Base	475	–	1.76	1.67
2	506	–	1.74	1.65
3	551	–	1.66	1.58
4	432	356	1.58	1.50
1	138	115	1.59	1.52

The ROI numbers are those from Fig. 11

The variations in substrate material can influence the energy distribution during laser treatment directly because of the different optical and thermal properties. It can also lead to varying properties of the layer generated during the coating process. Different wavelengths and pulse durations will always influence the spatial and temporal energy distribution in the sample, favouring different mechanisms of material degradation.

## 4 Conclusion

In summary, we have shown that a-C:H coatings are a very interesting model system to study the ablation and material modification effects of femtosecond laser pulses and electromagnetic radiation in general on thin coating materials, as the intrinsic optical and structural properties of the deposited films can be tuned over wide ranges. Specifically, we studied the effect of single near-infrared femtosecond laser pulses (35 fs duration, 800 nm wavelength) on two distinct types of sub-micrometre *semi-transparent* or *absorbing* a-C:H coatings, manufactured on silicon wafers by plasma-assisted chemical vapour deposition under different process conditions using a microwave (MW) and a high-frequency bias (RF) plasma source. Spectroscopic ellipsometry (SE) allowed us to quantify the optical constants of the pristine coating materials. Topometric and spectroscopic characterisations of the laser-irradiated sites by white light interference microscopy (WLIM), tactile stylus profilometry, and micro-Raman spectroscopy ( $\mu$ -RS) indicated structural material modifications in laser-modified zones for both types of coatings, manifesting through a reduced mass density as some tens of nanometre high mounds surrounding the ablation craters. While the absorbing (RF) coatings exhibited the expected surface ablation behaviour, the semi-transparent (MW) coatings showed characteristic step-like ablation profiles of  $\sim 250$  nm height ( $\approx \lambda/(2n)$ ) that can be explained by an intra-film separation. The latter originates from a standing light wave-based interference effect that is seeded and driven through the high-intensity fs-laser irradiation already during the laser pulse exposure before thermal effects set on. Finally, the analytic power of spectroscopic imaging ellipsometry (SIE) was demonstrated for our laser irradiated spots, even allowing a site-selective simultaneous quantification of the optical constants ( $n$ ,  $k$ ) along with the sub-micrometre film thicknesses that were previously not accessible by WLIM.

**Acknowledgements** We thank Gundula Hidde (BAM division 6.1) for helping with ellipsometry and other spectroscopic measurements as well as Simone Pentzien and Andrea Conradi (BAM division 6.2) for helping with optical microscopy and analysis. E.E. and A.H. thank Shun Okano, Matthias Duwe, and Stefan Schneider from Park Systems Germany for their constant support of our data analysis work. A.H.

thanks Grazia Daminelli for a very fruitful discussion about previous works in a-C:H laser processing.

A.H. and E.E. thank the ELENA project for funding the research at BAM. ELENA was supported by the European Metrology Programme for Innovation and Research under EMPIR 20IND12. The EMPIR initiative is co-funded by the European's Horizon 2020 Research and Innovation Programme and the EMPIR Participating States.

A.N.U. thanks the Karlsruhe School of Optics and Photonics (KSOP) and KIT / Land Baden-Württemberg as well as the Deutsche Forschungsgemeinschaft (DFG) for funding the femtosecond laser system used in this work under INST 121384/133-1FUGG.

**Author contributions** KH: laser experiments setup and laser experiments; microscopy, WLIM data analysis. JB: laser ablation analysis and interpretation. JK: additional aspects of laser ablation interpretation and discussion. MW: PA-CVD coating; WLIM measurements; Mechanical stylus profilometry measurements. EE: ellipsometry accuracy and calibration study, additional ellipsometry data processing. RS: Raman measurement and data analysis. ANU: concept of laser setup and laser treatment experiment, chief laser scientist. AH: main author and study leader, concept of the study, SE and SIE analysis, ellipsometry model development, ablation threshold analysis, WLIM and profilometer data analysis.

**Funding** Open Access funding enabled and organized by Projekt DEAL. Karlsruhe School of Optics and Photonics, Deutsche Forschungsgemeinschaft, INST 121384/133-1FUGG, Ministerium für Wissenschaft, Forschung und Kunst Baden-Württemberg, Andreas-Neil Unterreiner, European Metrology Programme for Innovation and Research, 20IND12 - ELENA, Andreas Hertwig.

**Data availability** Data from this article will be available under <https://doi.org/10.5281/zenodo.13928597> from Zenodo after publication.

**Declaration**

**Competing Interests** The authors declare no competing interests.

**Open Access** This article is licensed under a Creative Commons Attribution 4.0 International License, which permits use, sharing, adaptation, distribution and reproduction in any medium or format, as long as you give appropriate credit to the original author(s) and the source, provide a link to the Creative Commons licence, and indicate if changes were made. The images or other third party material in this article are included in the article's Creative Commons licence, unless indicated otherwise in a credit line to the material. If material is not included in the article's Creative Commons licence and your intended use is not permitted by statutory regulation or exceeds the permitted use, you will need to obtain permission directly from the copyright holder. To view a copy of this licence, visit <http://creativecommons.org/licenses/by/4.0/>.

## References





1. J. Robertson, Diamond-like amorphous carbon. *Mater. Sci. Eng.: R: Rep.* **37**(4–6), 129–281 (2002). [https://doi.org/10.1016/s0927-796x\(02\)00005-0](https://doi.org/10.1016/s0927-796x(02)00005-0)
2. M. Hiratsuka et al., Correlation between Optical Properties and Hardness of Diamond-Like Carbon Films. *J. Solid Mech. Mater. Eng.* **7**(2), 187–198 (2013). <https://doi.org/10.1299/jmmp.7.187>
3. A. Hertwig, J. Krüger, M. Weise, U. Beck, Hydrogen-containing amorphous carbon Layers as optical materials in the near-IR spectral range. *Plasma Process. Polym.* **4**, S76–S82 (2007). <https://doi.org/10.1002/ppap.200730406>

4. A. Grigonis, Ž. Rutkunienė, H. Manikowski, M. Šilinskas, Laser-induced transformation of a-C: H thin films. *Vacuum* **83**, S152–S154 (2009). <https://doi.org/10.1016/j.vacuum.2009.01.050>
5. A. Grigonis et al., Modification of amorphous a-C: H films by laser irradiation. *Lithuan. J. Phys.* **47**(3), 343–350 (2007). <https://doi.org/10.3952/lithjphys.47321>
6. J. Bonse, J. Krüger, Structuring of thin films by ultrashort laser pulses. *Appl. Phys. A* **129**(4), 14 (2023). <https://doi.org/10.1007/s00339-022-06229-x>
7. T.V. Kononenko et al., Effects of pulse duration in laser processing of diamond-like carbon films. *Diam. Relat. Mater.* **14**(8), 1368–1376 (2005). <https://doi.org/10.1016/j.diamond.2005.02.009>
8. K. Sokolowski-Tinten et al., Short-pulse-laser-induced optical damage and fracto-emission of amorphous, diamond-like carbon films. *Appl. Phys. Lett.* **86**(12), 121911 (2005). <https://doi.org/10.1063/1.1888037>
9. T.V. Kononenko et al., Laser-induced spallation in diamond-like carbon films. *Appl. Phys. A* **79**(3), 543–549 (2004). <https://doi.org/10.1007/s00339-003-2356-5>
10. R. Koter et al., Influence of film thickness and optical constants on femtosecond laser-induced ablation of hydrogenated amorphous carbon films. *J. Optoelectron. Adv. Mater.* **12**(3), 663–667 (2010)
11. N. Yasumaru et al., Laser-induced graphitized periodic surface structure formed on tetrahedral amorphous carbon films. *Diam. Relat. Mater.* **107**, 107909 (2020). <https://doi.org/10.1016/j.diamond.2020.107909>
12. S.M. Pimenov et al., Femtosecond-laser-ablation induced transformations in the structure and surface properties of diamond-like nanocomposite films. *Appl. Surf. Sci.* **509**, 144907 (2020). <https://doi.org/10.1016/j.apsusc.2019.144907>
13. K. Takabayashi et al., Morphology and structure of diamond-like carbon film induced by picosecond laser ablation. *Appl. Phys. A* **128**(9), 850 (2022). <https://doi.org/10.1007/s00339-022-05980-5>
14. N. Yasumaru, K. Miyazaki, J. Kiuchi, Glassy carbon layer formed in diamond-like carbon films with femtosecond laser pulses. *Appl. Phys. A* **79**(3), 425–427 (2004). <https://doi.org/10.1007/s00339-004-2746-3>
15. J. Budai et al., Preparation of hydrogenated amorphous carbon films from polymers by nano- and femtosecond pulsed laser deposition. *Appl. Surf. Sci.* **253**(19), 8235–8241 (2007). <https://doi.org/10.1016/j.apsusc.2007.02.138>
16. J. Budai, S. Tóth, Z. Tóth, M. Koós, Diamond-like carbon films prepared by reactive pulsed laser deposition in hydrogen and methane ambient. *Appl. Surf. Sci.* **253**(19), 8220–8225 (2007). <https://doi.org/10.1016/j.apsusc.2007.02.135>
17. J. Bonse et al., Femtosecond laser pulse irradiation effects on thin hydrogenated amorphous carbon layers. *Appl. Phys. A* **112**(1), 9–14 (2012). <https://doi.org/10.1007/s00339-012-7170-5>
18. Q. Wu et al., Raman investigation of amorphous carbon in diamond film treated by laser. *J. Appl. Phys.* **93**(1), 94–100 (2003). <https://doi.org/10.1063/1.1524306>
19. J. Wang et al., Microstructure and chemical bond evolution of diamond-like carbon films machined by femtosecond laser. *Appl. Surf. Sci.* **340**, 49–55 (2015). <https://doi.org/10.1016/j.apsusc.2015.02.169>
20. S.M. Pimenov et al., Femtosecond-laser surface modification and micropatterning of diamond-like nanocomposite films to control friction on the micro and macroscale. *J. Appl. Phys.* **122**(14), 145301 (2017). <https://doi.org/10.1063/1.4998586>
21. N.R. Arutyunyan, M.S. Komlenok, E.V. Zavedeev, S.M. Pimenov, Raman Spectroscopy of Amorphous Carbon Films Modified by Single-Pulse Irradiation of Nanosecond and Femtosecond Lasers. *Phys. Status Sol.* **255**(1), 1700225 (2017). <https://doi.org/10.1002/pssb.201700225>
22. M. Rybachuk et al., Near infrared optical materials from polymeric amorphous carbon synthesized by collisional plasma process. *Appl. Phys. Lett.* **96**(21), 211909 (2010). <https://doi.org/10.1063/1.3431292>
23. R.M.A. Azzam, Selected papers on ellipsometry, in *SPIE milestone series*. (SPIE Optical Engineering Press, Bellingham, WA, 1990)
24. R.M.A. Azzam, N.M. Bashara, *Ellipsometry and polarized light* (Oxford North-Holland, Amsterdam, 1977)
25. H. Fujiwara, *Spectroscopic ellipsometry principles and applications* (Wiley, NJ, 2007), p.369
26. M. Gioti, S. Logothetidis, The effect of substrate bias in amorphous carbon films prepared by magnetron sputtering and monitored by in-situ spectroscopic ellipsometry. *Diam. Relat. Mater.* **7**(2–5), 444–448 (1998). [https://doi.org/10.1016/s0925-9635\(97\)00297-5](https://doi.org/10.1016/s0925-9635(97)00297-5)
27. X. Zhou et al., Structural analysis of amorphous carbon films by BEMA theory based on spectroscopic ellipsometry measurement. *Diam. Relat. Mater.* **79**, 46–59 (2017). <https://doi.org/10.1016/j.diamond.2017.08.002>
28. C.M. Herzinger, B. Johs, W.A. McGahan, W. Paulson, A multi-sample, multi-wavelength, multi-angle investigation of the interface layer between silicon and thermally grown silicon dioxide. *Thin Solid Films* **313**, 281–285 (1998). [https://doi.org/10.1016/S0040-6090\(97\)00833-X](https://doi.org/10.1016/S0040-6090(97)00833-X)
29. C.M. Herzinger et al., Ellipsometric determination of optical constants for silicon and thermally grown silicon dioxide via a multi-sample, multi-wavelength, multi-angle investigation. *J. Appl. Phys.* **83**(6), 3323–3336 (1998). <https://doi.org/10.1063/1.367101>
30. G.E. Jellison, F.A. Modine, Parameterization of the optical functions of amorphous materials in the interband region (vol 69, pg 371, 1996). *Appl. Phys. Lett.* **69**(14), 2137–2137 (1996). <https://doi.org/10.1063/1.118155>
31. A.S. Ferlauto et al., Analytical model for the optical functions of amorphous semiconductors from the near-infrared to ultraviolet: Applications in thin film photovoltaics. *J. Appl. Phys.* **92**(5), 2424–2436 (2002). <https://doi.org/10.1063/1.1497462>
32. J. Bonse, S.M. Wiggins, J. Solis, T. Lippert, Phase change dynamics in a polymer thin film upon femtosecond and picosecond laser irradiation. *Appl. Surf. Sci.* **247**(1–4), 440–446 (2005). <https://doi.org/10.1016/j.apsusc.2005.01.125>
33. J. Bonse et al. Damage mechanisms in polymers upon NIR femtosecond pulse laser irradiation: sub-threshold processes and their implications for laser safety applications. International Symposium on High Power Laser Ablation, Santa Fe, (New Mexico), 2010: p. 56–64 <https://doi.org/10.1063/1.3507148>.
34. J.M. Liu, Simple technique for measurements of pulsed gaussian-beam spot sizes. *Opt. Lett.* **7**(5), 196–198 (1982). <https://doi.org/10.1364/Ol.7.000196>
35. V.V. Kononenko, Modification of diamond surface by femtosecond laser pulses. *Photonics* **10**(10), 1077 (2023). <https://doi.org/10.3390/photonics10101077>
36. J. Yin et al., Ablation mechanism investigation and ablation threshold prediction of single crystal diamond irradiated by femtosecond laser. *Diam. Relat. Mater.* **111**, 108173 (2021). <https://doi.org/10.1016/j.diamond.2020.108173>
37. K. Sokolowski-Tinten et al., Femtosecond laser-induced ablation of graphite. *Ultrafast Phenom* **XII**, 425–427 (2001)
38. S. Logothetidis et al., Stability, enhancement of elastic properties and structure of multilayered amorphous carbon films. *Appl. Surf. Sci.* **138–139**, 244–249 (1999). [https://doi.org/10.1016/s0169-4332\(98\)00401-2](https://doi.org/10.1016/s0169-4332(98)00401-2)
39. P. Lemoine et al., Intrinsic mechanical properties of ultra-thin amorphous carbon layers. *Appl. Surf. Sci.* **253**(14), 6165–6175 (2007). <https://doi.org/10.1016/j.apsusc.2007.01.028>

40. C. Casiraghi, A.C. Ferrari, J. Robertson, Raman spectroscopy of hydrogenated amorphous carbons. *Phys. Rev. B* **72**(8), 085401 (2005). <https://doi.org/10.1103/PhysRevB.72.085401>
41. C. Casiraghi et al., Bonding in hydrogenated diamond-like carbon by Raman spectroscopy. *Diam. Relat. Mater.* **14**(3–7), 1098–1102 (2005). <https://doi.org/10.1016/j.diamond.2004.10.030>
42. Q. Ding et al., An explanation for laser-induced spallation effect in a-C:H films: Altered phase evolution route caused by hydrogen doping. *J. Appl. Phys.* **109**(1), 013501 (2011). <https://doi.org/10.1063/1.3528223>
43. G. Dumitru et al., Femtosecond laser ablation of diamond-like carbon films. *Appl. Surf. Sci.* **222**(1–4), 226–233 (2004). <https://doi.org/10.1016/j.apsusc.2003.08.031>
44. A.C. Ferrari, J. Robertson, Interpretation of Raman spectra of disordered and amorphous carbon. *Phys. Rev. B* **61**(20), 14095–14107 (2000). <https://doi.org/10.1103/PhysRevB.61.14095>
45. M. Rybachuk, J.M. Bell, Electronic states of trans-polyacetylene, poly(p-phenylene vinylene) and sp-hybridised carbon species in amorphous hydrogenated carbon probed by resonant Raman scattering. *Carbon* **47**(10), 2481–2490 (2009). <https://doi.org/10.1016/j.carbon.2009.04.049>
46. M. Rybachuk, A. Hu, J.M. Bell, Resonant Raman scattering from polyacetylene and poly(p-phenylene vinylene) chains included into hydrogenated amorphous carbon. *Appl. Phys. Lett.* **93**(5), 051904 (2008). <https://doi.org/10.1063/1.2965458>
47. J.N. Hilfiker, T. Tiewald, Dielectric Function Modeling, in *Spectroscopic Ellipsometry for Photovoltaics : Volume 1: Fundamental Principles and Solar Cell Characterization*. ed. by R.W. Collins, H. Fujiwara (Springer International Publishing, NY, 2018), pp.115–153
48. B. Johs, J.S. Hale, Dielectric function representation by B-splines. *Phys. Status Sol. A* **205**(4), 715–719 (2008). <https://doi.org/10.1002/pssa.200777754>
49. J. Mohrmann et al., Application of a B-spline model dielectric function to infrared spectroscopic ellipsometry data analysis. *J. Vac. Sci. Technol. B* **38**(1), 014001 (2020). <https://doi.org/10.1116/1.5126110>
50. G. Daminelli, S. Pentzien, A. Hertwig, J. Krüger, Influence of film thickness on laser ablation of hydrogenated amorphous carbon films. *Appl. Phys. A* **83**(1), 89–94 (2005). <https://doi.org/10.1007/s00339-005-3460-5>

**Publisher's Note** Springer Nature remains neutral with regard to jurisdictional claims in published maps and institutional affiliations.

## Authors and Affiliations

Kenta Hirahara<sup>1</sup> · Jörn Bonse<sup>2</sup>  · Jörg Krüger<sup>2</sup>  · Matthias Weise<sup>2</sup> · Elena Ermilova<sup>2</sup> · Robert Schusterbauer<sup>2,3</sup> · Andreas-Neil Unterreiner<sup>1</sup>  · Andreas Hertwig<sup>2</sup> 

✉ Andreas Hertwig  
andreas.hertwig@bam.de

<sup>1</sup> Institute of Physical Chemistry, Karlsruhe Institute of Technology (KIT), Kaiserstraße 12, 76131 Karlsruhe, Germany

<sup>2</sup> Bundesanstalt für Materialforschung und -prüfung (BAM), Unter den Eichen 87, 12205 Berlin, Germany

<sup>3</sup> Freie Universität Berlin, Institute of Chemistry and Biochemistry, Altensteinstraße 23a, 14195 Berlin, Germany